Graph-based simulated annealing: A hybrid approach to stochastic modeling of complex microstructures

O Stenzel[1], D Westhoff[1], I Manke[2], M Kasper[3], D P Kroese[4] and V Schmidt[1]

[1]Institute of Stochastics, Ulm University
[2]Institute of Applied Materials, Helmholtz Center Berlin
[3]Centre for Solar and Hydrogen Research Baden-Württemberg (ZSW), Ulm
[4]Department of Mathematics, University of Queensland, Brisbane

E-mail: ole.stenzel@uni-ulm.de, daniel.westhoff@uni-ulm.de, manke@helmholtz-berlin.de, michael.kasper@zsw-bw.de, kroese@maths.uq.edu.au, and volker.schmidt@uni-ulm.de

Abstract. A stochastic model is proposed for the efficient simulation of complex 3-dimensional microstructures consisting of two different phases. The model is based on a hybrid approach, where in a first step a graph model is developed using ideas from stochastic geometry. Subsequently, the microstructure model is built by applying simulated annealing to the graph model. As an example of application, the model is fitted to a tomographic image describing the microstructure of electrodes in Li-ion batteries. The goodness of model fit is validated by comparing morphological characteristics of experimental and simulated data.

Submitted to: *Modelling Simulation Mater. Sci. Eng.*

PACS numbers: 02.50.Ng, 07.05.Tp, 82.47.Aa

1. Introduction

A stochastic 3D model for efficient simulation of complex microstructures is presented. It combines two well-established stochastic approaches: Spatial stochastic graphs and simulated annealing. First, a spatial stochastic graph model is developed which will describe the main structural features of the simulated microstructure. Then, a realization drawn from the graph model is discretized on a voxel grid, where voxels representing the edges of the graph are put 'white', and the remaining ones 'black'. Subsequently, the discretized graph is combined with simulated annealing in a second step. Therefore, the set of white voxels is filled up with further white voxels around the edges of the graph in order to get a suitable initial configuration for the simulated annealing algorithm. Thus, in the initial configuration, the white voxels tend to cluster along the edges of the graph. Note that the initial white voxels that represent the edges of the graph are not changed by simulated annealing and, therefore, they serve as a backbone for the simulated microstructure.

Standard simulated annealing is a popular tool to simulate microstructures. The basic idea is to start with a random allocation of black and white voxels (representing the respective phases) having predefined volume fractions. A Markov Chain Monte Carlo algorithm is used to coarsen this blend by randomly choosing a pair of neighboring voxels and probabilistically admitting a swap based on the energy of the system, where the energy is associated with its surface area. The advantage is that for model fitting, (mainly) two kinds of information are required: the specific surface area and the volume fraction. On the downside, computational times are rather large and the control on the geometric properties of the resulting microstructure is limited. In contrast, the combination of simulated annealing with the (fast) graph simulation leads to a stochastic simulation model with acceptable runtimes that is flexible to describe complex, experimentally measured microstructures.

The simulation model presented is this paper, is applied to the 3D microstructure of (uncompressed) graphite electrodes used in Li-ion batteries. In Thiedmann *et al.* (2011), another stochastic simulation model for (compressed) graphite electrodes used in Li-ion batteries, is proposed [4]. The idea of the model considered in Thiedmann *et al.* (2011) is to describe the compressed graphite electrode as a union of overlapping spheres with suitable correlation structure. The simulation model described in the present paper follows a different approach, where stochastic graph modeling is combined with simulated annealing. The advantage of this approach is that the volume fraction and the specific surface area can be easily adjusted or changed.

Application of stochastic nano- and microstructure models in the context of materials science has increased in the last years, ranging from proton exchange membrane fuel cells (PEMFC), solid oxide fuel cells (SOFC), organic solar cells, Li-ion batteries, Al-Si alloys, and foams [1–6]. The microstructure of these media is strongly determining their physical properties. In particular, the microstructure of porous media affects transport processes inside the medium, such as the maximum size of

particles that can be transported through the pore space. Considering organic solar cells, the nanostructure strongly affects the generation and transport of charges, i.e., their efficiency [7]. Regarding fuel cells, their properties and performance are also strongly connected to the 3D structure of the materials applied in these devices [8–12], where key issues are the optimization of catalysts materials and of gas diffusion media for optimized water / gas transport. Electron tomographic investigations show such correlations between catalysts properties and their 3D nanostructure [13, 14]. Often, however, a systematic understanding of the influence of the 3D microstructure on functional properties is missing. Stochastic models, fitted to experimental 3D image data, can help to elucidate this correlation between processing parameters, 3D microstructure, and functional properties. Furthermore, stochastic simulation models can be applied for virtual materials design, that is, to detect microstructures with improved functional properties. Such a design of virtual materials can be obtained by simulating a broad range of virtual microstructures according to the stochastic model (using different model parameters) and analysing their functional properties by numerical (transport) calculations.

With advancing progresses in the development and application of imaging methods like electron tomography [15], FIB / SEM tomography [16–19], X-ray / synchroton tomography [20,21] and neutron tomography [22], the demand for new methods, models and algorithms for 3D analysis of advanced energy materials is strongly increasing. Recently, tomographic studies have been applied to battery materials [23, 24]. As an example of application, the new approach proposed in this paper for stochastic model-based simulation of 3D microstructures is used to investigate the morphology of graphite electrodes in Li-ion batteries, where our simulation model has been fitted to experimental image data gained by synchrotron tomography. The original data set has a size of $624 \times 159 \times 376$ voxels with each single voxel representing 215 nm, where the white voxels represent the graphite phase. Since this data set has a relatively large size, our aim is to simulate a representative cutout of $100 \times 100 \times 100$ voxels and, in order to compensate this reduced size, implement periodic boundary conditions. Finally the simulation model is validated by comparing relevant image characteristics of experimental and simulated data, where a good agreement is found. Unless stated differently, all units are given in voxel.

The paper is organized as follows. The material and the applied imaging technique are described in Section 2. Then, in Section 3, the random graph model is explained. Section 4 deals with graph-based simulated annealing and its application to the simulation of microstructures. In particular, in Section 4.2, the implementation of simulated annealing on the graph model is discussed. Then, in Section 4.3, the graph-based simulation model is validated and, in Section 4.4, compared to other modifications of standard simulated annealing. The conclusions are given in Section 5.

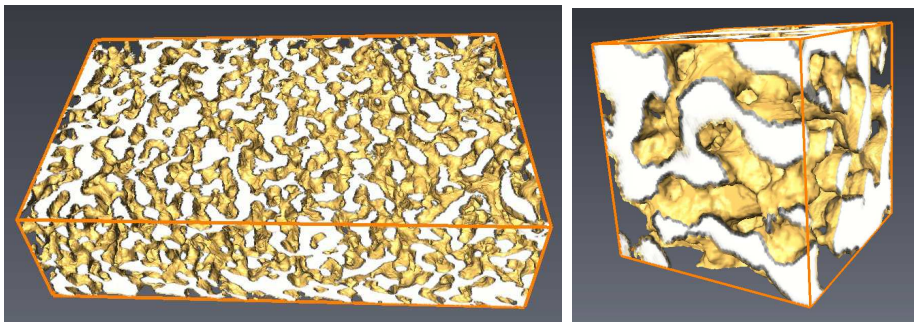

Figure 1. 3D image of experimental data (left) and cutout of $100 \times 100 \times 100$ voxels (right). The graphite phase appears yellow and the pore phase transparent.

2. Description of material and imaging technique

As an example of application, we fitted the stochastic simulation model proposed in the present paper to 3D image data that describe the microstructure of graphite electrodes in Li-ion batteries. The data set had a size of $624 \times 159 \times 376$ voxels with each voxel representing 215 nm. To get a visual impression of the microstructure of this material, see Figure 1.

The considered electrode material consisted of about 95% of graphite and of about 5% of a mixture of conductive carbon and PVDF (polyvinylidendifluoride) as binder material. The anode was located on both sides of a copper electrode with about $10 \pm 1\,\mu m$ thickness. The load was about $18.6 \pm 0,6\,mg/cm^2$ for both sides. The overall thickness of the measured sample was about $113\,\mu m$, i.e., the anode material had a thickness of about $50\,\mu m$ on both sides of the copper foil. The material was not loaded with lithium, i.e., raw material. The copper foil was not removed for the measurement in order to avoid any influence caused by sample preparation.

The measurements were performed at the synchrotron X-ray tomography facility at the BAMline (Bessy, HZB, Germany). The synchrotron X-ray beam was detected with a high resolution optical setup (Optique Peter, Optical and Mechanical Engineering France) and a PCO4000 CMOS camera with 4008×2672 pixel and a pixel size of $9\,\mu m$. A $20\,\mu m$ thick CWO scintillator screen was applied. The set-up provides a spatial resolution of $0.6\,\mu m$ at a pixel size of about $0.215\,\mu m$. The X-ray beam was monchromatized with a double multilayer monochromator (WSi) that provides an energy resolution of about $\frac{\Delta E}{E} \approx 10^{-2}$. An X-ray energy of $30\,keV$ was chosen (phase contrast tomography). Overall 1800 projections were taken. The exposure time was $3\,s$ for each radiographic projection image.

3. Random graph model

The basic idea of our modeling approach is to first simulate a random 3D graph which describes the essential structural properties of the underlying image data, and then to 'dilate' the graph by simulated annealing. Note that recently random 3D graphs

have been successfully used to describe the microstructure of various advanced energy materials [2, 25, 26].

A random geometric graph $G = (V, E)$ can be described by a random set of vertices $V = \{S_1, S_2, \ldots\}$, where S_i is the random location of the ith vertex in $\mathbb{R}^3$, and a random set of edges $E = \{(S_{i_1}, S_{j_1}), (S_{i_2}, S_{j_2}), \ldots\}$ describing the line segments between two connected vertices.

3.1. Extraction of 3D graph from experimental data

In order to fit the graph model to the microstructure of the tomographic image data described in Section 2, we first extracted a 3D graph from these data and then fitted the random graph model to the extracted graph. The graph extraction has been performed using a skeletonization algorithm provided by Avizo, see Figure 2. Note that for analysis purposes, an edge correction has been performed, where only those line segments are considered whose start- and endpoints are both contained within the image (bounding box).

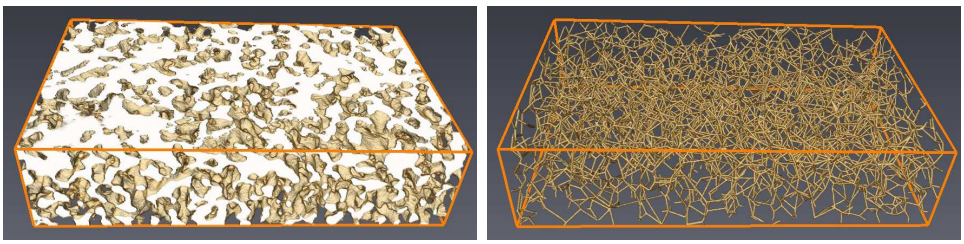

Figure 2. 3D image of experimental data (left) and extracted graph (right)

In order to find an appropriate graph model, several structural characteristics of the extracted graph have been analysed. First, the vertex set was analysed to find an appropriate point process which describes the set of vertices of the extracted graph sufficiently well. Then, the edge set of the extracted graph was investigated in the same way.

3.2. Stochastic modeling of vertices

3.2.1. Modulated hardcore point process We interpret the vertices of the extracted graph as a realization of a stochastic point process. To get an idea which class of point process models ht be suitable, we consider the pair-correlation function $g : (0, \infty) \to (0, \infty)$ of a stationary and isotropic point process in $\mathbb{R}^3$. Note that $g(r)$ is proportional to the relative frequency of point pairs with distance $r > 0$ from each other [27]. The pair correlation function of the point pattern of vertices of the extracted graph has been computed using a Gaussian kernel density estimator with a bandwith of 0.04, see Figure 3. For an automatic bandwidth estimation, see Botev *et al.* (2010) [28]. The fact that $g(r) = 0$ for small $r > 0$ clearly indicates a hardcore distance while $g(r) > 1$ for $2 < r < 7$ shows a strong clustering of points with 'medium' distances from each

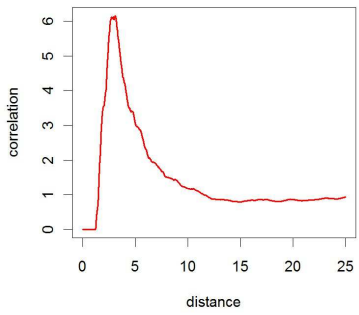

Figure 3. Estimated pair-correlation function

other. Therefore, a modulated hardcore point process appears suitable. This model can be described in the following way. Let $\{S_n^{(1)}, n \geq 1\}$ be a stationary Poisson process in $\mathbb{R}^3$ with intensity $\lambda^{(1)} > 0$. For any fixed $r_1 > 0$, the random set $\Xi = \bigcup_{n=1}^{\infty} B(S_n^{(1)}, r_1)$ is called a Boolean model, where $B(x, r) \subset \mathbb{R}^3$ denotes the sphere with centre $x \in \mathbb{R}^3$ and radius $r > 0$. Furthermore, let $\{S_n^{(2)}, n \geq 1\}$ be a stationary Matérn-hardcore process in $\mathbb{R}^3$ with intensity $\lambda^{(2)}$ and hardcore radius $r_h > 0$, where $\lambda^{(2)} = \lambda(1 - \exp(-\lambda^{(1)} \frac{4}{3}\pi r_1^3))^{-1}$ for some $\lambda > 0$; see Illian *et al.* (2008) for further details regarding Matérn-hardcore process [27]. Assume that the point processes $\{S_n^{(1)}\}$ and $\{S_n^{(2)}\}$ are independent. The stationary point process $\{S_n\} = \{S_n^{(2)}\} \cap \Xi$ is called a modulated hardcore process. Its intensity is equal to $\lambda > 0$, where only those points of $\{S_n^{(2)}\}$ are considered that belong to the system Ξ of overlapping spheres. In this way, a clustering of points for 'medium' distances is achieved, while a repulsion of points for 'small distances' is assured.

3.2.2. Model fitting The modulated hardcore point process $\{S_n\}$ can be described by four parameters: $\lambda, \lambda^{(1)}, r_1$ and r_h. Its intensity λ can be easily estimated by

$$\widehat{\lambda} = \frac{\text{total number of extracted vertices}}{\text{volume of sampling window}} .$$

Since r_h is the minimum distance between point pairs, we put this model parameter equal to the smallest distance between two extracted vertices. The remaining two parameters $\lambda^{(1)}, r_1$ are estimated by the minimum-contrast method with respect to the pair-correlation function, i.e.; $\lambda^{(1)}$ and r are chosen such that the discrepancy $\int_{r'}^{r''} (g(u) - g_{(\lambda^{(1)}, r_1)}(u))^2 \, du$ between the pair-correlation function g computed for the extracted vertices and its model counterpart $g_{(\lambda^{(1)}, r_1)}$ is minimized, where (r', r'') is a suitably chosen interval.

3.2.3. Model validation To get a visual impression of the goodness-of-fit, we refer to Figure 4, where three characteristics of the fitted modulated hardcore point process are displayed. Besides the pair-corrrelation function, the distribution functions of nearest-neighbor distances and spherical contact distances, respectively, are important (image)

characteristics which significantly influence the physical properties of the underlying materials [29]. Plots of these functions are shown in Figure 4, for both the extracted vertex points and the fitted point process. In general, we can observe a very good coincidence of these characteristics, although the peak of the pair-correlation function for the fitted point process is not as high as for the original data set. But nevertheless this (slightly lower) peak indicates strong clustering of points with medium distances from each other. The validation of the complete graph model, given in Section 3.4 below, shows that this little discrepancy of pair-correlation functions has no essential effect on the quality of the graph model and can therefore be neglected. On the other hand, the distribution functions of nearest-neighbor distances and spherical contact distances shown in Figure 4 fit perfectly.

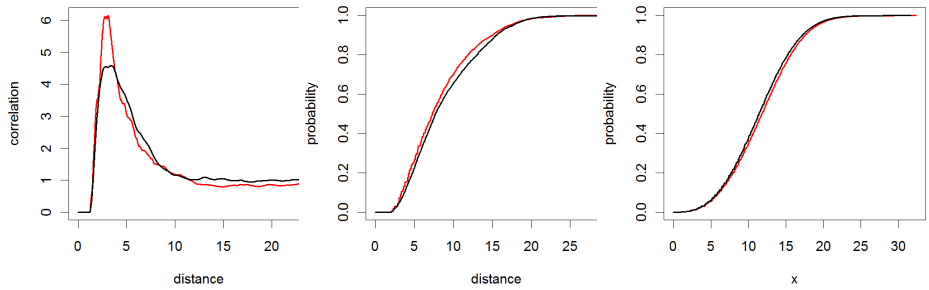

Figure 4. Pair-correlation function (left) and distribution function of nearest-neighbor distances (center) and spherical contact distances (right) for the fitted point process model (black) and extracted vertex points (red)

3.3. Stochastic modeling of edges

So far, we developed a stochastic model for the random set of vertices $V = \{S_1, S_2, ...\}$. For stochastic modeling of edges we consider the distribution of the minimum angle between neighboring edges, i.e., for an edge (S_i, S_j) that is emanating from vertex S_i we consider the smallest angle between (S_i, S_j) and all other edges emanating from S_i. In Figure 5 it can be seen that there is a tendency towards wider minimum angles between 50° to 60°.

3.3.1. Connecting nearest neighbors For each vertex $S_n \in V$, we consider its m nearest neighbors $\{S_n^{(1)}, ..., S_n^{(m)}\}$, where $S_n^{(i)}$ denotes the ith nearest neighbor of S_n. We then connect S_n with (some of) its m nearest neighbors according to the following rule, where E_n denotes the set of accepted edges: 1) Accept the shortest edge $(S_n, S_n^{(1)})$ and put $E_n = \{(S_n, S_n^{(1)})\}$. 2) Consider the next-nearest neighbour $S_n^{(2)}$. If the angle between $(S_n, S_n^{(2)})$ and every edge in E_n is larger than a certain threshold $\gamma_1 > 0$, then $(S_n, S_n^{(2)})$ is accepted and added to E_n, otherwise rejected. 3) Iteratively, repeat step 2 for $S_n^{(3)}, S_n^{(4)}, \ldots, S_n^{(m)}$.

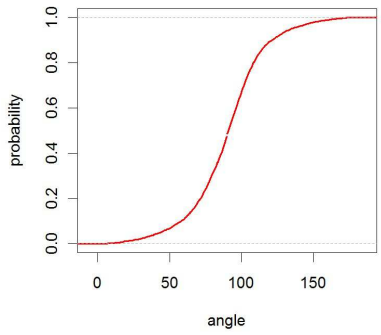

Figure 5. Distribution function of minimum angle between neighboring edges

This procedure is accomplished for every vertex S_n, which yields the set $E = \bigcup_{n=1}^{\infty} E_n$ of edges. As we want to implement periodic boundary conditions for the simulated annealing algorithm, this is already done for the graph model. Therefore, instead of considering the usual Euclidian distance, a modulo distance is used for computing the distance between two vertices. This means that edges hitting the boundary of the image are continued on the opposite site.

3.3.2. Postprocessing of edges In addition to the connection rule described above, we still perform a certain postprocessing of edges. The reason for this is that it can happen that $(S_i, S_j) \in E_i$ but $(S_j, S_i) \notin E_j$, although S_i belongs to the set of m nearest neighbors of S_j. This situation occurs if there is a vertex $S_k \in V$ with $|S_k - S_j| < |S_i - S_j|$ and $(S_j, S_k) \in E_j$ such that the angle between the edges (S_j, S_i) and (S_j, S_k) is smaller than γ_1.

To solve this problem we consider the following thinnning of edges. Let $(S_i, S_j) \in E$ be an arbitrary (undirected) edge. Then we perform a Bernoulli experiment in order to decide whether (S_i, S_j) is added to a list D of edges that are going to be deleted. Thus, putting $D = \emptyset$ at the beginning, we proceed as follows: 1) The angles between (S_i, S_j) and all edges of the form (S_i, S_k) and $(S_j, S_l) \in E$, where $k \neq i, l \neq j$, are calculated. 2) If at least one of these angles is less than a certain threshold $\gamma_2 > 0$, then (S_i, S_j) is added to D with probability of $p \in (0, 1)$. 3) Repeat steps 1 and 2 for each edge $(S_i, S_j) \in E$. 4) Take $E^* = E \setminus D$ as the final edge set.

The stochastic edge model introduced above has four parameters: m, γ_1, γ_2, and p, which have been determined using the minimum-contrast method with respect to the distributions of edge lengths, edge-angles, coordination numbers and spherical contact distances. As the result we received $m = 10, \gamma_1 = 90°, \gamma_2 = 80°$ and $p = 5\%$.

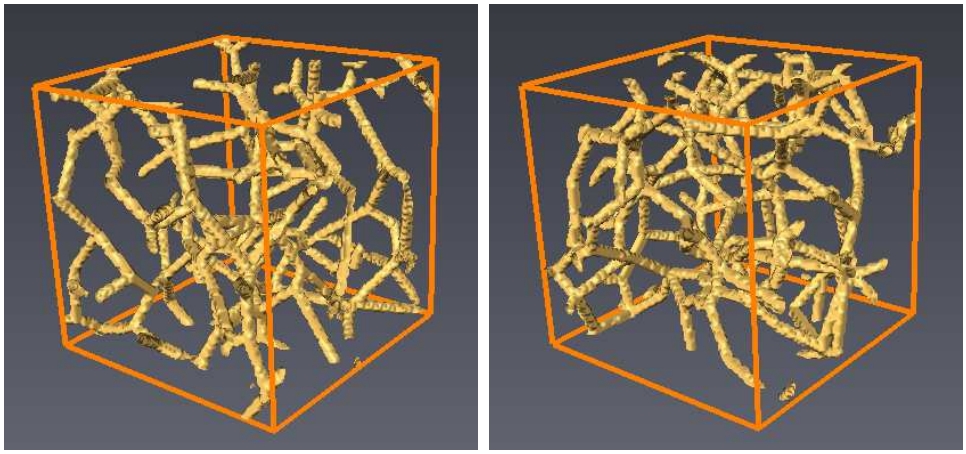

Figure 6. Graph extracted from original data (left) and simulated graph (right)

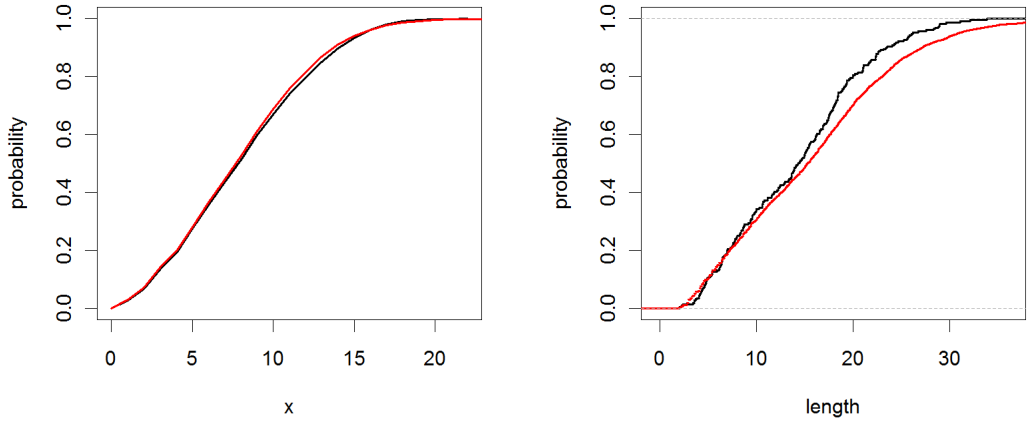

Figure 7. Distribution function of spherical contact distances (left) and edge lengths (right) for the fitted graph model (black) and the graph extracted from experimental data (red)

3.4. Model validation

To get a visual impression of the goodness-of-fit, in Figure 6 a cutout of the 3D graph extracted from experimental data is shown, together with a (simulated) realization of the random graph model. Since the experimental graph, displayed in Figure 6 (left), is a cut-out, the simulated graph (Figure 6 (right)) is also a cutout of a larger observation window.

Furthermore, the goodness-of-fit of the random graph is validated by comparing structural characteristics of the graphs extracted from experimental data and simulated from the graph model, respectively. In particular, we consider the distribution functions of spherical contact distances, edge lengths, minimum angles between edges, and coordination numbers. For all these characteristics, a good agreement has been obtained

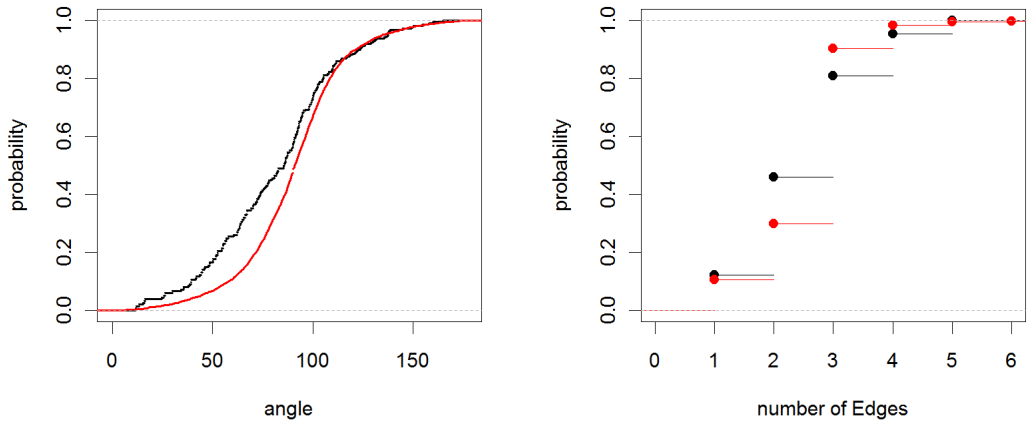

Figure 8. Distribution function minimum angles between edges (left), and coordination numbers (right) for the fitted graph model (black) and the graph extracted from experimental data (red)

between results for original and simulated graphs; see Figures 7 and 8.

4. Graph-based simulated annealing

Simulated annealing is a well-established stochastic optimization algorithm with a wide field of applications, such as the traveling-salesman problem, image segmentation, graph partitioning; see Kroese *et al.* (2011) for an introduction to this field [30]. It is also a standard method to generate two-phase (or multiple-phase) morphologies on a voxel lattice that are often used as input of physical simulations. Among many other applications, simulated annealing is used to describe the microstructure of sandstones, metals, and organic solar cells [7]. In this section, we briefly describe the basic idea of the simulated annealing algorithm and its specific implementation for the generation of 3D morphologies.

4.1. Standard algorithm

The basic idea of standard simulated annealing is to start with a random distribution of black and white voxels on a voxel lattice with the same volume fractions as in some orginal image data, and define a cost function. This may be, for example, the surface area of the white voxel, various correlation functions, or the squared sum of different cost functions. Then, two (normally neighboring) voxels are picked at random and exchanged, where the value of the cost function of both the previous and the changed image are computed. If the cost function decreases due to the exchange, the exchange is accepted, otherwise it is only accepted with a certain probability. The acceptance probability depends on the energy of the old and new configuration as well

as a temperature. During the course of the simulation the temperature is changed gradually according to the cooling schedule. This leads to a structure where voxel are ordered in a special way depending mostly on the chosen cost function but also on the cooling schedule.

More precisely, consider a set W of voxel representing the sampling window, and $I = \{I(x), x \in W\}$ a binary image on W. Suppose that at the beginning we have $I(x) = 0$ for each $x \in W$ (black voxel). Furthermore, by α_0 we denote the volume fraction and by β_0 the value of the cost function of the experimental data set, whereas $\alpha(I)$ is the volume fraction of white voxels in I and $\beta(I)$ the value of the cost function of I. Let T denote the initial temperature, M the number of iterations per step, and c a decrease factor for the temperature T. Finally, we write $\beta_{x,y} = \beta(I_{x,y})$ where $I_{x,y} = \{I_{x,y}(z), z \in W\}$ is a binary image such that $I_{x,y}(x) = I(y)$, $I_{x,y}(y) = I(x)$ and $I_{x,y}(z) = I(z)$ for any $z \neq x, y$. Then, the standard simulated annealing algorithm can be described as follows: 1) Perform Bernoulli experiments to throw white voxels(i.e. $I(x) = 1$) into W according to the uniform distribution until the volume fraction α_0 is reached, i.e. $\alpha(I) = \alpha_0$. 2) As long as $\beta(I) > \beta_0$, repeat the following steps: (a) Set $m = 1$ and repeat the steps (b) to (d) until $m = M$. (b) Pick two voxels x, $y \in W$ at random such that $I(x) \neq I(y)$. (c) If $\beta_{x,y} - \beta(I) \leq 0$, swap $I(x)$ and $I(y)$, otherwise swap $I(x)$ and $I(y)$ only with probability $\exp(-(\beta_{x,y} - \beta(I))/T)$. (d) Set $m = m + 1$ and continue with (b). (e) After M steps, set $T = c \cdot T$. Go to (a) if $\beta(I) > \beta_0$.

Note that especially for larger window sizes run times are rather large and simulated annealing only provides a limited control of the resulting microstructure. Therefore, with standard simulated annealing, only small cutouts of 3D microstructures can be simulated reasonably and improvements of the algorithm are desirable. In the next section, we propose an approach which enables us to simulate 3D microstructures for window sizes of $100 \times 100 \times 100$ voxels much faster than this is possible with standard simulated annealing.

4.2. Combination of graph model and simulated annealing

Standard simulated annealing as described in Section 4.1, can be used to generate 3D morphologies, but run times are rather large. Moreover, since only two parameters can be adjusted (the values α_0 and β_0 of volume fraction and cost function, respectively), this algorithm offers only limited control of the resulting morphology of white and black voxels. In fact, it turns out that the standard simulated annealing algorithm does not describe the microstructure of the experimental image data considered in the present paper sufficiently well, especially for larger window sizes.

We therefore propose another, more efficient approach, which we call graph-based simulated annealing, where first a random 3D graph is simulated as explained in Section 3, which is then combined with simulated annealing. Thereby the graph describes the essential morphological properties of the considered microstructure and serves as a backbone for the simulated annealing algorithm.

4.2.1. Initial configuration Instead of throwing uniformly distributed white voxels into the sampling set W, an initial configuration of white voxels is constructed which the previously simulated graph. The idea is as follows: The simulated 3D graph is discretized on the lattice W, i.e., we put $I(x) = 1$ for those voxels $x \in W$ that belong to the graph, and $I(x) = 0$ for those voxels that do not belong to the graph. This discretized graph indicates voxels around which further white voxels will be located until the volume fraction α_0 is reached.

To take the most important advantage of our graph-based approach into account, we require that each white voxel of the initial configuration is connected to the graph. Therefore, we first choose a voxel $x \in W$ at random. Then, we choose a random direction (parallel to the x-, y-, or z-axis) and decide at random if we want to go forward or backward into this direction. Thus, there are six directions where each of them can be chosen with probability 1/6. Along the selected direction, we move from $x \in W$ until we either reach a white voxel representing the graph or another (white) voxel that has been placed there in an earlier step (and therefore is connected to the graph). Finally, we put the voxel at the currently reached location to 'white'. This procedure is continued until $|\{x \in W : I(x) = 1\}|/|W| = \alpha_0$.

If a voxel and direction is chosen that we hit the boundary of W before reaching any white voxel, then that this choice is discarded and we start with a new one. In this way, we get an initial configuration where every white voxel is connected to the graph. In Figure 9 we can see the difference to the initial configuration of the standard simulated annealing algorithm, where voxels are thrown at random into the window according to the uniform distribution.

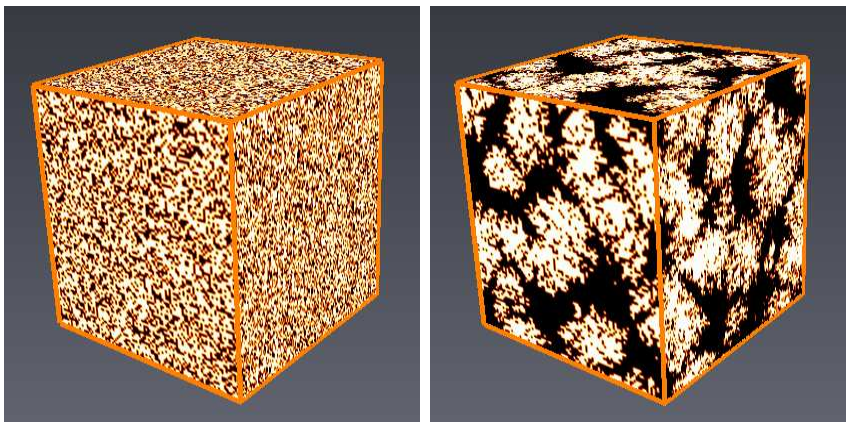

Figure 9. Initial configuration of standard (left) and graph-based (right) simulated annealing

Note that the value of the cost function corresponding to the initial configuration described above is typically much closer to the value β_0 of the cost function corresponding to the experimental data set than the value of the cost function corresponding to a purely random initial configuration. This is one reason why graph-based simulated annealing is much faster than the standard version of this algorithm.

4.2.2. Description of graph-based algorithm Besides the different ways to create initial configurations, there are two further important differences between standard and graph-based simulated annealing. First, (white) voxels representing the discretized graph may not be swapped. Therefore, the discretized graph serves as 'rock' and white voxels tend to cluster around it, where the graph forms the skeleton of the morphology to be simulated. In this way, i.e., first simulating a random 3D graph and then applying simulated annealing, one can nicely control the resulting morphology.

Consider a window W of size $100 \times 100 \times 100$, and $I = \{I(x), x \in W\}$ a binary image on W which displays the graph, i.e., $I(x) = 1$ if x belongs to the graph and $I(x) = 0$ otherwise. Furthermore, let α_0 be the volume fraction of the foreground phase of experimental data, and β_0 its surface area (which we use as cost function). Analogously, let $\alpha(I)$ be the volume fraction of white voxels in I and $\beta(I)$ the surface area of I. As initial temperature we choose $T = 0.3$, which is a value where enough changes are accepted. The number M of iterations per step is chosen proportional to the window size (in our case $M = 0.1 \times |W|$), and the cooling factor c for the temperature T is put equal to $c = 0.98$ [31]. Finally, like in Section 4.1, we write $\beta_{x,y} = \beta(I_{x,y})$ where $I_{x,y} = \{I_{x,y}(z), z \in W\}$ is a binary image such that $I_{x,y}(x) = I(y)$, $I_{x,y}(y) = I(x)$ and $I_{x,y}(z) = I(z)$ for any $z \neq x, y$. Then, the standard simulated annealing algorithm can be described as follows:

(i) Fill up W with white voxels as described in Section4.2.1, until the volume fraction α_0 is reached, i.e. $\alpha(I) = \alpha_0$.

(ii) As long as $\beta(I) > \beta_0$, repeat the following steps:
   (a) Set $m = 1$, $\beta_{old} = \beta(I)$ and repeat the steps (b) to (d) until $m = M$.
   (b) Choose two neighbouring voxels x, $y \in W$ (with respect to the 26-neighbourhood), which do not belong neither to the same phase nor to the graph.
   (c) If $\beta_{x,y} - \beta(I) \leq 0$, swap $I(x)$ and $I(y)$, otherwise swap $I(x)$ and $I(y)$ only with probability $\exp(-(\beta_{x,y} - \beta(I))/T)$.
   (d) Set $m = m + 1$ and continue with (b).
   (e) After M steps, set $T = c \cdot T$ if $(\beta_{old} - \beta(I))/\beta_{old} < 5 \times 10^{-6}$. Go to (a) if $\beta(I) > \beta_0$.

Note that in contrast to the standard simulated annealing algorithm as described in Section 4.1, we postulate a slightly different condition for the decrease of the temperature T. It is not necessarily changed after M steps but only if the additional condition that $(\beta_{old} - \beta(I))/\beta_{old} < 5 \times 10^{-6}$ is fulfilled [31]. As in Sections 3.3.1 and 4.2.1, periodic boundary conditions are implemented, i.e., swaps over the boundary of the sampling window W are possible. For the computation of surface area, an algorithm described in Ohser and Mücklich (2000) is used [32]. Note that in each iteration step, the surface area has to be calculated to evaluate if a swap of voxels is desired. Here, it is sufficient to only calculate the surface area for a small cutout, which considerably enhances runtime.

4.2.3. Simulation result In Figure 10 an initial configuration of graph-based simulated annealing is compared with the corresponding (final) image obtained by this algorithm. We see that in the final simulation result there are clusters of the foreground phase at the same locations as in the initial configuration. Furthermore, it is clearly visible in Figure 10 that the graph-based algorithm has nicely smoothed the microstructure of the initial configuration.

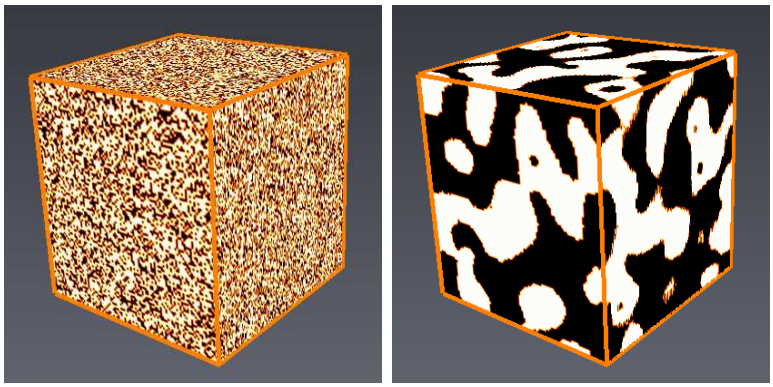

Figure 10. Initial configuration (left) and final result (right) of graph-based simulated annealing

4.3. Model validation

The goal of this paper is to develop a method in order to efficiently simulate the microstructure of graphite electrodes as displayed in Figure 1. We therefore combined the simulation of random 3D graphs with simulated annealing, where we were matching the volume fraction α_0 and the specific surface area β_0 of the experimental image data. Figure 11 gives a visual representation of the goodness-of-fit which can be achieved by the graph-based simulated annealing described in the previous sections of this paper.

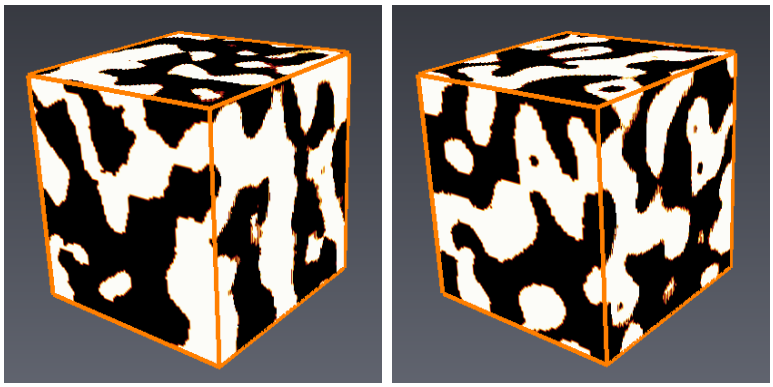

Figure 11. Experimental data (left) and 3D microstructure obtained by graph-based simulated annealing (right)

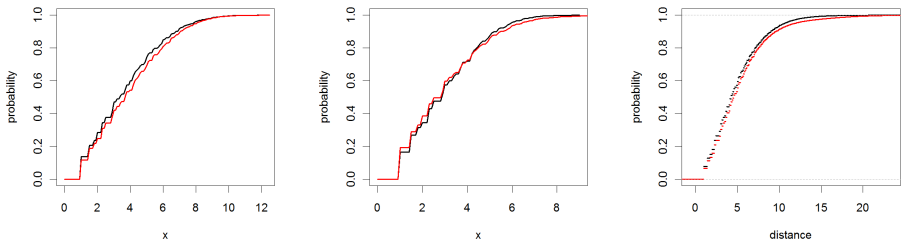

Figure 12. Distribution function of spherical contact distances from pore phase to foreground (left) and vice versa (center) for simulated (black) and experimental (red) data. Right: spherical contact distances for the graphs from the edges of the graph to the pore phase

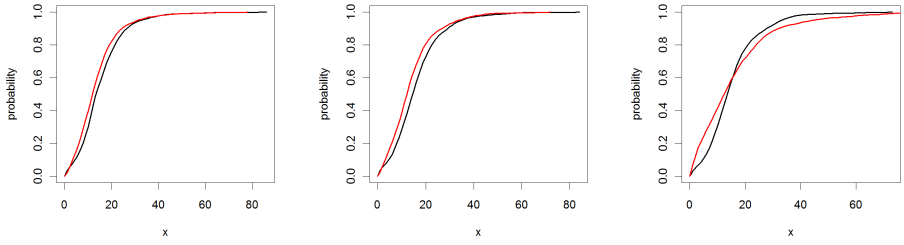

Figure 13. Distribution function of chord lengths along the x- (left), y- (center) and z-axis (right) for simulated (red) and experimental (black) data

To formally validate the result of graph-based simulated annealing with respect to the 3D morphology of graphite electrodes, we compared several structural characteristics for both experimental and simulated data. To begin with, we computed the distribution functions of spherical contact distances from the pore phase to the foreground, and vice versa. The results displayed in Figure 12 show an excellent agreement between experimental and simulated data. The same good fit holds true for the chord-length distribution functions shown in Figure 13. Furthermore, we compared the distribution functions of spherical contact distances from the graph to boundary of the microstructure. More precisely, for each (white) voxel from the graph, we compute the distance to the nearest pore-phase (i.e., black) voxel. Thus, we describe the spatial elongation of the microstructure, from the point of view of the graph. The results in Figure 12 (right) show that this characteristic is also perfectly fitted.

Last but not least, for the application of the stochastic simulation model developed in the present paper to the microstructure of graphite electrodes, it must be assured that the graph-based simulated annealing resembles the main connectivity properties of the considered material. Note that the graphite electrode will be completely connected. In the 3D image data, however, it can occur that bridges between graphite particles are smaller than the resolution and therefore, isolated clusters may appear. Also, isolated clusters at the boundary may be connected with the electrode via bridges outside of

the observation window. Therefore, we made a cluster analysis for both, a cut-out of $130 \times 130 \times 130$ voxels of the 3D experimental image data and for a corresponding simulation, see Figure 14. It turns out that 95.54% of experimental 3D graphite electrode is connected, in comparison to 100% for the stochastic model.

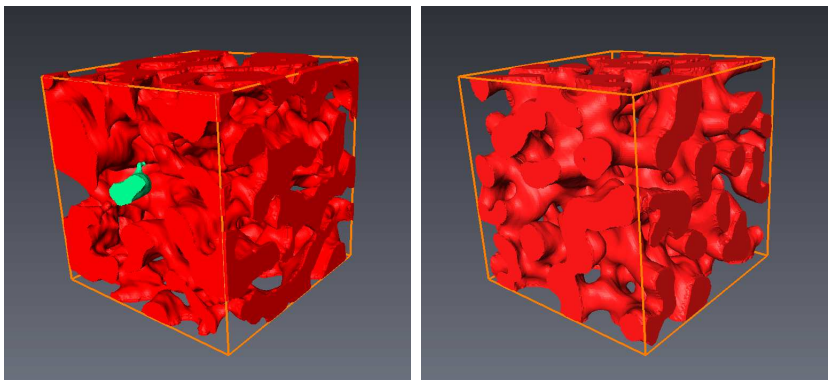

Figure 14. Connectivity of graphite electrode: Cut-out of 130^3 voxels from experimental data (left) and corresponding simulation (right). Different clusters are marked by different colours.

4.4. Comparison to other algorithms

In the literature, there are many different approaches to improve the standard simulation annealing algorithm, ranging from changing the choice of voxels that are exchanged [33], the combination of simulated annealing with other algorithms [34], to exchanging spheres instead of pixels/voxels [35]. To give a comparison, for a 100^3 voxels, the graph-based simulated annealing with optimized starting allocation required 11 hours, compared to 74 hours for graph-based simulated annealing with 'normal' starting allocation. Standing simulated annealing did not converge to the desired specific surface area within a week.

In addition to the possibility to perform simulations within large windows and respectable runtimes, our graph-based simulated annealing can adequately reproduce the morphological properties of complex 3D microstructures like those of the electrode material described in Section 4.3. This is due to the fact that our approach consists of three steps: First, a stochastic point process model is fitted which describes the vertices of the underlying 3D graph. Then, the edge model is fitted to experimental data and, finally, the graph-based simulated annealing is performed. After every step, the goodness-of-fit is validated, so that the final simulation results fit very well to experimental data.

What is also remarkable is the simplicity of the cost function considered in the graph-based simulated annealing algorithm. In other approaches, rather sophisticated image characteristics like correlation functions or different distribution functions are chosen as a cost function, sometimes even the sum of more than one squared cost function is considered [35].

In our approach, we only need to optimize the surface area. The simplicity of this cost function allows us to compute their values merely for a local cutout of the current image, because the surface area changes only in small surroundings of two neighboring voxel.

5. Conclusions

In the present paper, a stochastic 3D model for efficient simulation of complex microstructures has been proposed, which combines two well-established stochastic approaches: graph simulation and simulated annealing. Whereas standard (global) simulated annealing is a rather slow algorithm with limited control of the resulting microstructure, the combination with the (fast) graph simulation leads to a stochastic simulation model with acceptable runtimes and good fits of complex microstructures. Thereby, the graph nicely controls the characteristics of the simulated microstructure as it describes the essential structural properties of the underlying material.

As an example of application, our approach has been used in order to investigate the morphology of graphite electrodes in Li-ion batteries, where the graph-based simulation model has been fitted to experimental image data gained by synchrotron tomography. The original data set has a size of $624 \times 159 \times 376$ voxesl with each single voxel representing 215 nm. Since this data set has a relatively large size, we considered a representative cutout of $100 \times 100 \times 100$ voxels and, in order to compensate this reduced size, implemented periodic boundary conditions. The simulation model has been validated by comparing relevant image characteristics of experimental and simulated data.

Acknowledgments

We kindly acknowledge funding from the DAAD (Germany Academic Exchange Service) under the programme ‘Go8’.

References

[1] Gaiselmann G, Thiedmann R, Manke I, Lehnert W and Schmidt V 2012 Stochastic 3D modeling of fiber-based materials *Comput. Mater. Sci.* **59** 75–86

[2] Gaiselmann G, Neumann M, Holzer L, Hocker T, Prestat M and Schmidt V 2013a Stochastic 3D modeling of LSC cathodes based on structural segmentation of FIB-SEM images *Comput. Mater. Sci.* (in print)

[3] Stenzel O, Koster L J A, Thiedmann R, Oosterhout S D, Janssen R A J and Schmidt V 2012 A new approach to model-based simulation of disordered polymer blend solar cells *Adv. Funct. Mater.* **22** 1236–44

[4] Thiedmann R, Stenzel O, Spettl A, Shearing P R, Harris S J, Brandon N P and Schmidt V 2011 Stochastic simulation model for the 3D morphology of composite materials in Li-ion batteries *Comput. Mater. Sci.* **50** 3365–76

[5] Gaiselmann G, Stenzel O, Afonina A, Muecklich F and Schmidt V (2013b) Competitive stochastic growth model for the 3D microstructure of eutectic Si in Al-Si alloys Preprint (submitted)

[6] Redenbach C, Wirjadi O, Rief S and Wiegmann A 2011 Modelling a ceramic foam for filtration simulation *Adv. Eng. Mater.* **13**(3) 171–77

[7] Watkins P, Walker A, and Verschoor G 2005 Dynamical Monte Carlo modelling of organic solar cells: The dependence of internal quantum efficiency on morphology *Nano Lett.* **5** 1814–18

[8] Gerteisen D, Heilmann T, and Ziegler C 2008 Enhancing liquid water transport by laser perforation of a GDL in a PEM fuel cell *J. Power Sources* **177**(2) 348–54

[9] Hartnig C, Jörissen L, Kerres J, Lehnert W and Scholta J 2008 Polymer electrolyte membrane fuel cells (PEMFC) In: *M. Gasik (ed.), Materials for Fuel Cells* (Cambridge: Woodhead Publishing) 101–84

[10] Krüger P, Markötter H, Haussmann J, Klages M, Arlt T, Banhart J, Hartnig C, Manke I, and Scholta J 2011 Synchrotron tomography for investigations of water distribution in PEM fuel cells *J. Power Sources* **196**(12) 5250–55.

[11] Markötter H, Manke I, Krüger P, Arlt T, Haussmann J, Klages M, Riesemeier H, Hartnig C, Scholta J, and Banhart J 2011 Investigation of 3D water transport paths in gas diffusion layers by combined in-situ synchrotron X-ray radiography and tomography *Electrochem. Commun.* **13**(9) 1001–04

[12] Mathias M F, Roth J, Fleming J and Lehnert W 2003 Diffusion media materials and characterisation In: *W. Vielstich, A. Lamm and H. Gasteiger (eds.), Handbook of Fuel Cells* (London: J. Wiley & Sons) 517–37

[13] Leary R, Saghi Z, Armbruster M, Wowsnick G, Schlogl R, Thomas J M, and Midgley P A 2012 Quantitative high-angle annular dark-field scanning transmission electron microscope (HAADF-STEM) tomography and high-resolution electron microscopy of unsupported intermetallic GaPd2 catalysts *J. Phys. Chem. C* **116**(24) 13343–52

[14] Schulenburg H, Schwanitz B, Linse N, Scherer G G, Wokaun A, Krbanjevic J, Grothausmann R, and Manke I 2011 3D Imaging of catalyst support corrosion in polymer electrolyte fuel cells *J. Phys. Chem. C* **115**(29) 14236–43

[15] Midgley P A and Dunin-Borkowski R E 2010 Electron tomography and holography in materials science *Nat. Mater.* **8** 271–80

[16] Dunn D N and Hull R 1999 Reconstruction of three-dimensional chemistry and geometry using focused ion beam microscopy *Appl. Phys. Lett.* **75** 3414–16

[17] Holzer L and Cantoni M 2012 Review of FIB-tomography In *I. Utke, S. A. Moshkalev and P. Russel (eds.), Nanofabrication using Focused Ion and Electron Beams: Principles and Applications* (New York: Oxford University Press) 410–35

[18] Inkson B J, Steer T, Mobus G and Wagner T 2001 Subsurface nanoindentation deformation of Cu-Al multilayers mapped in 3D by focused ion beam microscopy *J. Microsc.* **201** 256–69

[19] Zils S, Timpel M, Arlt T, Wolz A, Manke I, and Roth C 2010 3D visualisation of PEMFC electrode structures using FIB nanotomography *Fuel Cells* **10**(6) 966–72

[20] Banhart J, Borbely A, Dzieciol K, Garcia-Moreno F, Manke I, Kardjilov N, Kaysser-Pyzalla A R, Strobl M and Treimer W 2010 X-ray and neutron imaging - complementary techniques for materials science and engineering *Int. J. Mater. Res.* **101**(9) 1069–79

[21] Stock S R 2008 Recent advances in X-ray microtomography applied to materials *Int. Mater. Rev.* **53** 129—81

[22] Kardjilov N, Manke I, Hilger A, Strobl M and Banhart J 2011 Neutron imaging in materials science *Mater. Today* **14**(6) 248–56

[23] Manke I, Banhart J, Haibel A, Rack A, Zabler S, Kardjilov N, Hilger A, Melzer A, and Riesemeier H 2007 In situ investigation of the discharge of alkaline Zn-MnO_2 batteries with synchrotron x-ray and neutron tomographies *Appl. Phys. Lett.* **90**(21) 214102.

[24] Shearing P R, Howard L E, Jorgensen P S, Brandon N P and Harris S J 2010 Characterization of the 3-dimensional microstructure of a graphite negative electrode from a Li-ion battery *Electrochem. Commun.* **12**(3) 374–77

[25] Baumeier B, Stenzel O, Poelking C, Andrienko D and Schmidt V 2012 Stochastic modeling of molecular charge transport networks Preprint (submitted)

[26] Thiedmann R, Manke I, Lehnert W and Schmidt V 2011 Random geometric graphs for modeling the pore phase of fibre-based materials *J. Mater. Sci* **46** 7745–59

[27] Illian J, Penttinen A, Stoyan H and Stoyan D 2008 *Statistical Analysis and Modeling of Spatial Point Patterns* (Chichester: J. Wiley & Sons)

[28] Botev Z I, Grotowski J F and Kroese D P 2010 Kernel density estimation via diffusion *Ann. Stat.* **38**(5) 2916–57

[29] Oosterhout S D, Wienk M M, van Bavel S S, Thiedmann R, Koster L J A, Gilot J, Loos J, Schmidt V and Janssen R A J 2009 The effect of three-dimensional morphology on the efficiency of hybrid polymer solar cells *Nat. Mater.* **8** 818–24

[30] Kroese D P, Taimre T and Botev Z I 2011 *Handbook of Monte Carlo Methods* (New York: J. Wiley & Sons)

[31] Laarhoven P J M and Aarts E H L 1987 *Simulated Annealing: Theory and Applications* (Dortrecht: Kluwer Academic Publisher)

[32] Ohser J and Mücklich F 2000 *Statistical Analysis of Microstructures in Materials Science* (Chichester: J. Wiley & Sons)

[33] Tang T, Teng Q, He X and Luo D 2009 A pixel selection rule based on the number of different-phase neighbours for the simulated annealing reconstruction of sandstone microstructure *J. Microsc.* **234** 262–68

[34] Patelli E and Schueller G 2009 On optimization techniques to reconstruct microstructures of random heterogeneous media *Comput. Mater. Sci.* **45** 536–49

[35] Diogenes A N, dos Santos L O E, Fernandes C P, Moreira A C and Apollon C R 2009 Porous media microstructure reconstruction using pixel–based and object–based simulated annealing – comparison with other reconstruction methods *Engenharia Térmica* **8** 35–41